ZIBELINE INTERNATIONAL™ PUBLISHING

ISSN: 2521-5035 (Print)
ISSN: 2521-5043 (Online)
CODEN: ESMACU

Earth Sciences Malaysia (ESMY)

DOI: http://doi.org/10.26480/esmy.02.2021.104.113

RESEARCH ARTICLE

LOVE SURFACE WAVES AND ELECTRICAL RESISTIVITY USED TO DELINEATE THE NEAR SURFACE GEOPHYSICAL STRUCTURE: THEORETICAL CONSIDERATIONS

Özcan Çakır[a], Nart Coşkun[b]

[a]Süleyman Demirel University, Department of Geophysics, Isparta, TURKEY.
[b]Cumhuriyet University, Department of Geophysics, Sivas, TURKEY.
**Corresponding Author email: ozcancakir@sdu.edu.tr; nartcoskun@cumhuriyet.edu.tr*

ARTICLE DETAILS

Article History:

Received 05 October 2021
Accepted 10 November 2021
Available online 11 November 2021

ABSTRACT

We invert Love surface waves and electrical resistivities to cooperatively examine the physical properties of the depth range shallower than 50-m. To analyze this depth range is essential for earthquake mitigation efforts. The shear-wave velocity (V_{S30}) is particularly important to describe the dynamic characteristics of shallow Earth. The Love surface waves are treated in terms of both phase and group velocities. The phase velocities are obtained from the slant stacking while for the group velocities the multiple filter technique is utilized. A typical shot-gather is assumed to simulate the field collection of the surface wave data. The phase velocity curve represents the average structure beneath the geophone spread. The group velocity curve represents the average structure from the source to the geophone. In a single-station fashion, for each geophone location one group velocity curve is obtained. A linear system is set up to convert these single-station group velocity curves into local group velocity curves at grid points. The latter group velocities are inverted to attain the shear-wave velocity cross section. A similar approach is adopted to study the electrical resistivity structure of the underground. We simulate the field application using a theoretical model. Multiple electrode Pole-Pole array is assumed for the field collection of the resistivity data. The apparent (measured) resistivity values are inverted to attain the true resistivity structure in terms of a cross section. The inverted structures are one-dimensional reflecting depth dependent shear-wave velocities and electrical resistivities underneath the studied region.

KEYWORDS

Electrical resistivity, inversion, Love surface waves, near surface, single station

1. INTRODUCTION

The physical properties of the near surface structure are major concern for engineering and economic geology, civil engineering, environmental, and archaeological investigations. The prospected depth range may change from a few meters to a few thousand meters from the surface. The field surveys reaching depths of a few thousand meters are primarily designed to detect the occurrences of ore minerals and hydrocarbon fuels as well as geothermal and groundwater resources (Kana et al., 2015). In case of building large-scale engineering structures such as transportation tunnels, subways, suspension bridges, the depth range to explore the foundation may extend from a few tens of meters to hundred meters (Bačić et al., 2020). In archeological and environmental studies, topmost a few meters of the Earth are mostly investigated (Dumont et al., 2017). The geophysical methods (i.e., seismic, electrical, gravity, magnetics, and electromagnetics) are frequently employed to measure the needed physical parameters (e.g., elasticity modules, anisotropy, attenuation, density, electrical conductivity, magnetic permeability) of the Earth. The measurements are mostly made by instruments deployed at the free surface, inside the drilled wells and at the ocean bottom. The collected data are then solved to characterize the underground structure (Bitri et al., 2013; Gao et al., 2018; Pan et al., 2019; Pan et al., 2020; Mi et al., 2020).

A particular geophysical method is only sensitive to certain physical properties of the investigated media. For instance, the seismic method is primarily sensitive to elastic parameters expressed by P (compression) and S (shear) velocities of the propagating media while the density is secondarily effective in the wave propagation. The gravity method may help distinguish between dense ore deposits and lighter host rock. On the other hand, the electrical resistivity method is primarily sensitive to porosity, permeability, groundwater, salinity, conductive and resistive mineral content of the media. Insufficient sensitivity of a particular method along with limited data may result in the non-uniqueness of the geophysical inversion. Different geophysical methods applied in an integrated manner may help alleviate the sensitivity problem while improving the inversion quality (Gaždová et al., 2015). In this respect, different seismic methods (i.e., reflection, refraction, and surface waves) may be jointly employed to determine the velocity structure beneath the survey area (Onyebueke et al., 2018; Senkaya et al., 2020). The latter approach providing more data and different perspective to the project is likely more beneficial than that one of these methods is applied alone in the field. Sedimentary basins with certain alluvial buildup above the bedrock pose earthquake hazard since seismic waves may spend more time in these basin valleys through which multiply reflections and refractions bounce back from the basin boundaries (Furumura et al., 1997). The basin geometry and the respective layered structure could be examined using seismic and gravity methods (Silahtar et al., 2020).

Quick Response Code	Access this article online	
	Website: www.earthsciencesmalaysia.com	**DOI:** 10.26480/esmy.02.2021.104.113

Cite The Article: Özcan Çakır, Nart Coşkun (2021). Love Surface Waves and Electrical Resistivity Used To Delineate The Near Surface Geophysical Structure: Theoretical Considerations.*Earth Sciences Malaysia, 5(2): 104-113.*

Love surface waves and electrical resistivity method have found many applications in geosciences (Ronczka et al., 2017; Çakır et al., 2019; Chianga et al., 2021). We cooperatively consider these two data sets to interpret the subsurface underneath an interested area. For the seismic data we consider a classical shot-gather (i.e., combination of single shot and linear geophone array). Traditionally surface waves recorded on such a geophone array are analyzed to get the phase velocity dispersion curve using the method of Multichannel Analysis of Surface Waves and then the corresponding dispersion curve is inverted to attain the one-dimensional (1-D) S-wave velocity-depth profile representing the average seismic velocity structure beneath the geophone spread (Xia et al., 1999; Park et al., 2001; Yuan et al., 2014). The MASW method is non-invasive and cost-effective as it is applied either in a passive or active fashion in the field. In case of active application, the seismic source is a vibroseis, sledgehammer or weight drop. The passive version (ReMi) carried out along different geophone arrays (i.e., lines, circles, rectangles, triangles) utilizes cultural or ambient noise (human and industrial activities, construction, cars, machines, winds, waves) as vibration sources (Silahtar and Kanbur, 2021; Pancha and Apperley, 2021). We consider the active MASW, and additionally single-station (group velocity) approach frequently applied in earthquake seismology.

Relevant to this work there exist many studies in the literature employing both surface wave and electrical resistivity methods to image the subsurface. For instance, some researchers have utilized full waveform inversion of SH – horizontally polarized shear-waves and Love surface waves to determine the near-surface Earth structure (Yan et al., 2020). In a similar work, have investigated the near-surface structure beneath a location with archaeological significance by applying full waveform inversion of SH- and Love-wave data (Schwardt et al., 2020). A group researcher has jointly employed dispersion curves of both Rayleigh and Love surface waves to determine the shear-wave velocities of shallow Earth materials (Yin et al., 2020). Some researchers have utilized three-dimensional electrical resistivity tomography to study the hydrothermal structure beneath the Solfatara Crater in Italy (Gresse et al., 2017). Pawlik and Kasprzak have employed the electrical resistivity tomography to investigate the biomechanical effects of trees (Pawlik and Kasprzak, 2018). Some researchers have used the electrical resistivity tomography to image the deep three-dimensional structure beneath the Campi Flegrei caldera in Italy (Troiano et al., 2019).

Herein we are primarily interested in imaging the layered geophysical structure within the topmost 50 m or shallower Earth. This depth range is especially critical for assessing the earthquake hazard in a region, i.e., foundation shear strength characterized by V_{S30} (Borcherdt, 2012; Thitimakorn and Raenak, 2016; Hollender et al., 2018). We first discuss how the Love surface waveforms are treated to obtain the (phase and group velocity) dispersion curves and then the inversion strategy on these dispersion curves to attain the shear-wave velocity structure is outlined. The Love surface waves representing the actual waveforms propagating in the Earth are simulated by forward solutions using a representative Earth model. The same strategy is followed for the electrical resistivity inversion, i.e., forward computation of representative (calculated or apparent) resistivities on a layered resistivity model and then inversion of apparent resistivities for structural assessment.

2. SH-Waves and Electrical Resistivity: Methods

A geophysical survey includes three main steps, i.e., field measurements (surveying), data processing (inversion), and interpretation of results for geological structure principally characterized by existence, location, shape, and size. The most suitable geophysical method (s) must be chosen so that the fundamental understanding of the physical properties of the geological target and the surrounding media are properly established. The measurement could be occasionally performed on a laboratory sample collected from the field. However, the result could be quite different from in situ measurement since the laboratory conditions may not exactly simulate the real conditions in the field. Herein we consider theoretical modeling of in situ measurements.

2.1 Love surface waves inversion

The seismic surface waves primarily sensitive to S-wave (shear) velocities are frequently used in exploring the velocity structure in the Earth (Erduran et al., 2007; Çakır, 2019). The Rayleigh surface waves consist of constructive interference of P (compressional) and SV waves (vertically polarized) multiply refracted and reflected in a layered half-space. There are also wave-type conversions from P-to-SV and SV-to-P. On the other hand, the Love surface waves, which we currently consider, also include multiply refracted and reflected waves in a layered half-space, but the constructive interference takes place between SH waves (horizontally polarized) (Xia et al., 2012). A sledgehammer vertically hitting the surface creates Rayleigh surface waves propagating near the surface within the ground. To create Love surface waves is somewhat challenging since the sledgehammer must be used to deliver a horizontal impact onto an object (e.g., concrete or metal block) firmly pushed against the surface laying down horizontally. There exist various source systems to create SH-waves used in the reflection, refraction, MASW studies (Haines 2007; Vanneste et al., 2011; Wright, 2012; Lawton et al., 2013; Mahvelati et al., 2021). Figure 1 illustrates the shot-gather geometry along with the SH-wave source and the horizontal geophones.

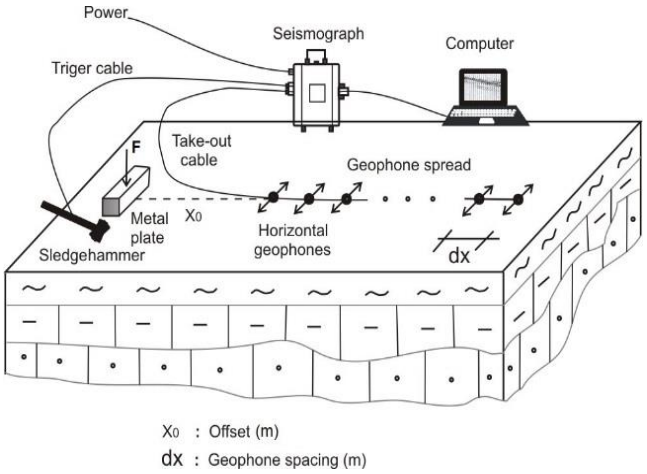

Figure 1: SH-wave field acquisition geometry. SH-wave energy source (a sledgehammer horizontally hitting the metal plate) and horizontal geophones are used. The metal plate is firmly pushed against the ground by the application of the vertical force F. Both source and receivers (geophones) are placed on the surface.

To model Love surface waves could be performed by seeking a fit between the observed and the calculated waveforms in which these source parameters regarding the source type (i.e., double-couple, single force, or explosion), source time history, magnitude, depth, offset, and attenuation are needed (Kasamatsu et al., 2021). Another method, which is independent of the source information, is to model the dispersion curves extracted from the waveforms. We employ the second approach where both phase and group velocity dispersion curves are employed. The surface waves are composed of fundamental mode plus higher modes. In the modeling, to include the higher modes, which have greater vertical propagation depth compared to the fundamental mode, can significantly improve the resolution power of the inversion (Shapiro et al., 2001; Xu and Beghein, 2019).

By employing the Multichannel Analysis of Surface Waves (MASW) we extract the phase velocity dispersion curve from a common-shot wave gather (Figure 1). The related method was proposed where an array of seismic traces is slant stacked in the $p-\tau$ domain (i.e., phase slowness-intercept time) and then transformed into the spectral $p-\omega$ domain by Fourier transform over the intercept time (McMechan and Yedlin, 1981). The stacking procedure in includes the superposition of multiple surface wave modes (Mokhtar et al., 1988). The phase velocity stack values plotted as a two-dimensional (2-D) function of p and ω show the largest values from which the phase velocity dispersion curve of a particular mode is picked (Herrmann, 2002; Çakır et al., 2019). To attain the phase velocity dispersion curve, we also utilize the weighted preconditioned Linear Radon Transform – LRT on the shot gather. Compared to the slant stacking – SS, the LRT is shown to enhance the resolution in the dispersion image by more than 50% (Luo et al., 2008).

After the phase velocity curve is obtained using the MASW over an array of geophones, we move to analyzing the individual waveforms recorded at each geophone. The group velocity dispersion curve representing the average wave propagation between the source and the geophone is obtained in a single-station fashion frequently applied in earthquake seismology. We employ the Multiple Filter Technique – MFT to extract the group velocity dispersion curve from the observed waveform (Dziewonski et al., 1969; Herrmann, 1973). The narrow-band Gaussian filter $exp[-\alpha(f-f_c)^2/f_c^2]$ is used to filter the observed waveforms in the frequency domain where f_c is the filter center frequency. Here, $\alpha = 35$ is the filter parameter trading off resolution between the frequency and time domains. The phase velocity curve is inverted to obtain the 1-D velocity structure beneath the geophone array and then this velocity structure is utilized as initial model in the iterative least-squares inversions of the group velocity curves. In this way, one phase velocity

curve (i.e., MASW) and multiple group velocity curves (i.e., single-station approach) are cooperatively utilized to delineate the velocity structure laterally beneath the geophone array.

2.2 Electrical resistivity tomography

The electrical resistivity studies have found many applications in geophysics such as determining the depth of bedrock and mapping its relief, exploring the strength of sedimentary layers for foundations, identifying the sedimentary layers, prospecting for groundwater, studying the ancient underground cities, and determining the geometry of a landslide (Coşkun et al., 2016b; Cardarelli and Donno, 2017; Kowalczyk et al., 2017; Crook et al., 2008; Issah et al., 2018; Coşkun et al., 2016a). The method is based on mapping the conductivity anomalies arising from differences between adjacent rock units. Figure 2 shows some typical resistivities of rocks, minerals, and other Earth materials. The subsurface geology includes rock units with conductivities changing from highly conductive (less than 1 Ω m in cases of sulfide accumulates associated with volcanic activity or graphite) to highly resistive (over 1000 Ω m in cases of metamorphic and igneous rocks). Values outside these ranges in Figure 2 are also possible depending on the specific field conditions (Palacky, 1988).

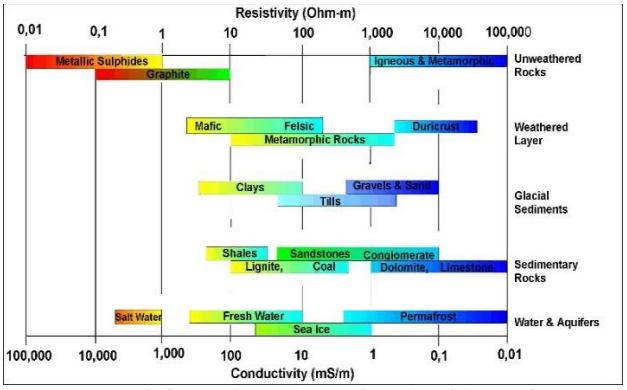

Figure 2: Typical electrical resistivity values found for Earth materials (Carbajal, 2014; Palacky, 1988).

The deeper weathered layer between the water table and the bedrock surface (i.e., saprolite) has the resistivities in the range 2-200 Ω m. The weathered layer near the surface above the water table is less conductive with resistivities in the range 200-2000 Ω m. The duricrust with thickness in the range from a few millimeters or centimeters to several meters is highly resistive (between 2000 and 30000 Ω m). The glacial sediments with gravel, sand and tills show resistivities in the range 50-10000 Ω m while clays accumulated in lakes developed after the withdrawal of glaciers are conductive (5 to 100 Ω m). In case of sedimentary rocks where the electrical resistivity spans a wide range, the electrical conductivity depends on several properties of the media such as clay and other minerals content, porosity, water saturation. For instance, shales more conductive than limestones, dolomites, and conglomerates (1000 to 100000 Ω m) have a rich clay content that causes low resistivity (5 to 30 Ω m).

The basic data collection method in the field includes two electrodes used to inject a direct or a low frequency alternating current to the ground supplied by a battery or some other source of electric power. An ammeter connected to these two current electrodes is used to measure the amount of current flow in the system. Two other electrodes at some distinct locations are attached to the ground to measure (via a voltmeter) the potential differences created by the electrical resistivity structure in the Earth. A geometric factor, which is a function of positions of current and potential electrodes, is utilized to convert the measured potential difference into (apparent) resistivity value. Such a reading with this four-electrode array is repeated at many different locations at the surface from which a pseudo cross-section is constructed (Coşkun, 1994). Modern geophysical applications employ Electrical Resistivity Tomography – ERT where the pseudo cross-section measured via a multichannel and multielectrode system (see Figure 3) is inverted into the subsurface resistivity distribution (Stummer et al., 2002; Colella et al., 2004).

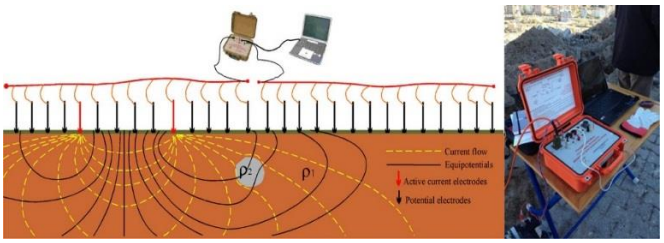

Figure 3: A representative sketch of a multichannel and multielectrode system typically used in electrical resistivity measurements (Coşkun et al., 2016a).

We utilize a synthetic model made of multiple layers over a half-space and calculate the consequent electrical response on the surface using the RES2DMOD forward modeling program (Loke, 1997; Orlando, 2013). The model is considered to represent the electrical resistivity-depth profiles in the real Earth. The apparent resistivity pseudo-section response, which is noise free, is then treated as input data for the inversion program RES2DINV (Loke, 1997). An electrode spacing greater than required, target depth, resistivity difference between the target and the host media, and noise are those issues that may cause resolution weaknesses in the inversion (Coşkun et al., 2016a). A traditional data collection technique uses certain configuration of current and potential electrodes (e.g., Dipole-Dipole, Schlumberger or Wenner array). Alternatively, all possible electrode configurations of data may be merged into a particular dataset that allows collection of large amounts of data substantially enhancing the resolve of the subsurface inversion (Coşkun et al., 2016a and 2016b).

3. Numerical Results

The real Earth has a multi-layered structure. The layer interfaces may show one-dimensional (flat), two-dimensional (dipping), or three-dimensional (topographic) variations and within each layer there may exist three-dimensional heterogeneities (i.e., inclusions such as sinkhole, cavity, ore body, salt, melt, fluid). In fault zones, the layered structure is deformed across compressive, tensional, and shearing forces where the layer interfaces are folded and displaced by reverse faults (compressive), normal faults (tensional) or strike-slip faults (Roche et al., 2020). There exist shallow Earth structures showing complex geological formations created by various tectonic forces (more specifically fold-and-thrust belts), (Poblet and Lisle, 2011). For these geologically complex regions one needs to employ diverse techniques including three-dimensional seismic, computer and laboratory modelling to image the main structural features. Herein we focus on relatively simple Earth structure that could be approximated by 1-D model. In our modeling effort, we are mainly interested in how accurately the thickness, depth, and physical parameter (i.e., shear-wave velocity or electrical resistivity) of a layer are inverted. We assume that the Earth structure is measured via the group and phase velocities of Love surface waves and the electrical resistivity. We select 1-D model to test the effectiveness of these data in delineating the surveyed Earth structure.

3.1 Inversion results for the model structure

The model structure as listed in Table 1 is designed to represent the lithologic variation in an alluvial deposit, which includes relatively young unconsolidated sediments (i.e., erosional clay, silt, sand, and gravel) deposited in a sorted manner by water flow. The multi-layered model is assumed to have eight layers with 40-m thickness over the half space. The model structure is described by layer thickness, shear-wave velocity (Vs), density, shear-wave quality factor (Q_S) and electrical resistivity.

3.1.1 Love surface waves modeling

Surface wave propagation includes multiple modes, i.e., fundamental mode plus higher modes. Currently we utilize only fundamental mode – FM and those effects from higher modes in the waveforms are suppressed through the applied procedures in the data processing. If the separation of the FM from the higher modes is impossible, then the observed (or extracted) dispersion curve may be different than the actual one (Levshin and Panza, 2006; Gao et al., 2016). The FM energy travels close to the free surface where the depth penetration increases with increasing period or wavelength (Ojo et al., 2017). The higher modes propagate deeper than the FM and hence a deeper seismic source excites more higher mode energy than a source near the free surface (Nishida et al., 2008). In earthquake seismology, it is a common practice to utilize shallow earthquakes (i.e., focal depth ≤ 50 km) to alleviate the interference problem of higher modes in the surface wave dispersion analysis for the seismic structure (Jin and Gaherty, 2015).

Table 1: Model of alluvial deposits. The layered resistivity model is prepared based on the observations (Amaya et al., 2016). The shear-wave velocities – Vs are adopted from (Kanlı et al., 2006).

Layer number	Thickness (m)	Vs (m/s)	Density (gr/cm^3)	Quality factor (Q_S)	Resistivity (Ω m)	Lithology
1	5	200	1.6	80	400	Topsoil
2	5	350	1.8	80	50	Clay and Sand
3	5	450	1.8	100	200	Sand and Clay
4	5	500	1.8	100	130	Gravel and Sand
5	5	550	1.8	100	100	Gravel and Sand
6	5	600	1.9	100	300	Gravel
7	5	750	1.9	120	50	Sand and Clay
8	5	800	1.9	140	50	Sand and Clay
9	∞	850	1.9	160	30	Clay

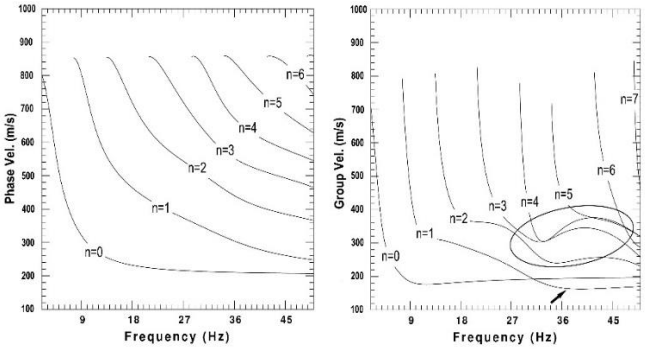

Figure 4: Phase (left panel) and group (right panel) velocity dispersion curves for the model structure in Table 1 are shown. The fundamental mode – FM is labeled n=0 and then higher modes are labeled with increasing numbers, i.e., n=1, n=2, n=3, and so on.

We utilize the source code package to compute the surface wave observables, i.e., dispersion curves and synthetic seismograms (Herrmann, 2002). The same code package is also utilized for extracting the phase and group velocity dispersion curves and inverting these dispersion data for the velocity-depth profile via the damped least-squares. The phase and group velocity curves are obtained by using the slant stacking and multiple filter technique, respectively (McMechan and Yedlin, 1981; Dziewonski et al., 1969; Herrmann, 1973). In Figure 4, we present the multimode phase and group velocity dispersion curves conforming to the Love surface waves propagating in the model structure. The frequency band ranges from 2 Hz to 50 Hz in which there exist seven dispersion curves, i.e., fundamental mode plus six higher modes. The phase and group velocities in the range 100-1000 m/s are shown on the left and right panels, respectively. The phase velocity curves are well separated from each other and there does not exist any mode kissing event (Gao et al. 2016). The group velocity curves are also separated, but there exist some higher modes mingling at high frequencies (>27 Hz) and low group velocities (<400 m/s – see the ellipse). The mode mixing between different modes (i.e., fundamental, and first higher) around group velocity of 200 m/s at high frequencies (>31 Hz – see the black arrow in Figure 4) causes interference problem as explained below. In Figure 5, we show the synthetic seismograms consistent with SH-waves propagating in the model structure. The minimum offset and the geophone spacing (constant) are both set to 2-m. The source and the receivers (geophones) with linear alignment are placed on the surface (see Figure 1) where the wavefield sampled at 0.0025 s is recorded by 48 horizontal geophones with maximum offset set to 96-m.

Figure 6 (left panel) shows the result of slant stacking – SS applied to the synthetic seismograms illustrated in Figure 5. The fundamental mode – FM phase velocity curve extracted by the SS is indicated by a white line connecting black dots marking the red color area (maximum stack) on the dispersion image. The result of Linear Radon Transform – LRT with weighting and preconditioning as applied to the synthetic seismograms in Figure 5 is shown in Figure 6 on the right panel where the theoretical multi-mode phase velocity curves corresponding to the model structure are shown by these blue lines superimposed on the dispersion image. The fit between the solid circles and the first blue line (right panel) shows that the FM phase velocity curve is estimated well for frequencies greater than ~5 Hz. Some first higher mode energy is also evident for frequencies greater than ~38 Hz as indicated by the black arrow. Therein the blue color arrow indicates the interference effect by the first higher mode while the red color arrow shows how the FM dispersion curve is disturbed by this interference. In Figure 5, the first geophone is located at 2-m, and the last geophone at 96-m, which corresponds to a lateral extent of 94-m represented by the FM phase velocity curve shown in Figure 6. In case that the Earth structure beneath the geophone array is heterogeneous, then this dispersion curve characterizes the average structure.

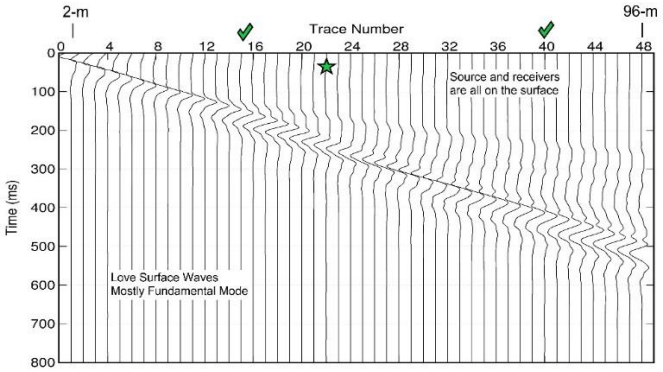

Figure 5: Seismic traces showing SH body waves and Love surface waves corresponding to the model structure in Table 1. See text for more explanation.

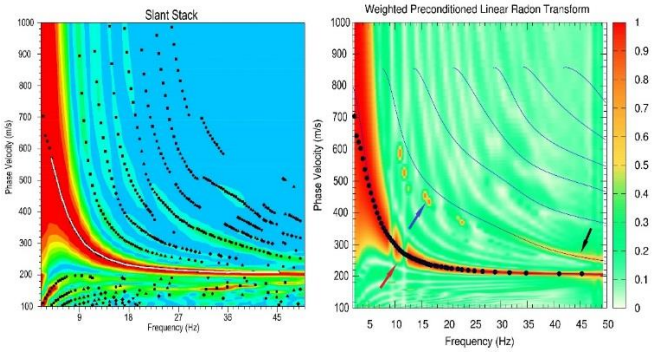

Figure 6: Phase velocities in the model structure (Table 1) computed from seismograms in Fig. 5 are shown. The left panel corresponds to the method of slant stacking (white line). In the right panel, the method of linear radon transform weighted and preconditioned is used (solid circles).

In Figure 7, we show the inversion results corresponding to the FM phase velocity curve in Figure 6. The inversion procedure is 1-D and utilizes the damped least-squares technique. Herein we omit the details regarding the inversion method that can be found elsewhere (Herrmann 2002; Çakır, 2018). The 1-D inversion is iterative that is initiated from a simple model of multiple layers having velocities gradually increasing from 800 m/s at the surface to 900 m/s in the half-space (blue color dashed line in Figure

7). The resulting velocity-depth profile fitting the theoretical (or observed) dispersion values (open circles) is given by the red color line. We consider noise free conditions in the current inversions and thus a perfect dispersion fit between the theoretical (open circles) and inverted (red color) is obtained. The latter model structure is used as initial in the following 1-D inversions based on the group velocity curves.

The FM phase velocity curve in Figure 6 is obtained by the multichannel analysis of surface waves (MASW) using two analogous methods (i.e., SS and LRT). Now we move to the analysis of surface waves using the classical single-station approach where the surface wave recording at each geophone is individually treated to attain the FM group velocity curve corresponding to the pathway from the source to the receiver. This procedure, which requires the source information, gives us multiple FM group velocity curves corresponding to the multiple recording geophones. The source timing (or zero time) is accurately transmitted to the seismograph through the trigger cable, and the source and geophone locations are measured according to a coordinate system set up in the field (see Figure 1). Depending on the development of constructive interference, the high frequency (or short wavelength) surface waves are first created near the source and then the frequency band extends to these low frequencies (or long wavelengths) with propagation gradually away from the source. The wavelength determines the depth penetration of surface waves, i.e., surface waves travel deeper with increasing wavelength.

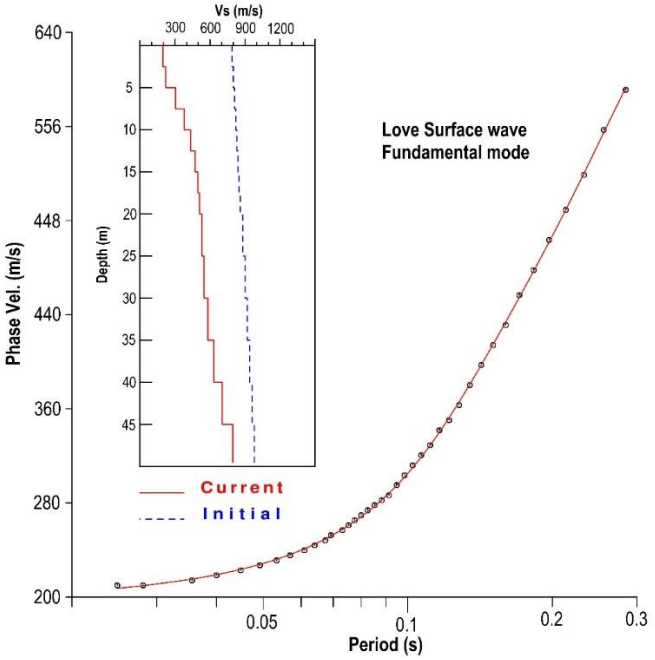

Figure 7: 1-D inversion result for the phase velocity curve in Figure 6 is shown. Vs stands for the shear-wave velocity (m/s). The horizontal axis shows the period (s).

For the single-station analysis we utilize surface wave recordings at receivers in the distance range 30-80 m, i.e., currently these geophones numbered from 15 to 40 (see the check marks in Figure 5). The long wavelength surface waves at distances shorter than 30-m are not well developed hindering the resolution of the deep structure. On the other hand, the short wavelength surface waves at distances longer than 80-m are more attenuated resulting low resolution of the velocity structure near the surface. Therefore, the distance range selected as 30-80 m is evaluated optimal to constrain the 40-m thickness above the half-space in the model structure. In case that the target depth extends deeper than 40-m, then these geophones at distances longer than 80-m are required in the dispersion analysis to consider amplitudes with relatively longer wavelengths. In Figure 8, we show the result of multiple filter technique – MFT applied to the recording at 44-m distance (i.e., geophone #22 indicated by a star – see Figure 5). Since a detail of MFT is provided elsewhere, we only show the MFT results herein (Herrmann, 2002). The FM group velocity curve (white line) is obtained by connecting the solid squares marking the middle of the red color area (maximum amplitudes) on the dispersion image. Before applying the MFT, the surface wave spectral amplitudes $|F(\omega)|$ were treated using the following functional, which helps boost the week amplitudes.

$$\tilde{F}(\omega) = \frac{|F(\omega)|e^{j\varphi(\omega)}}{|\bar{F}(\omega)|^{\gamma} + \delta} \quad (1)$$

In Eq. (1), $\delta = mean|F(\omega)| * 5/100$ is the pre-whitening factor and $\gamma = 0.5$ chosen from the range $0 \leq \gamma \leq 1$. If $\delta \gg |F(\omega)|^{\gamma}$, then $\tilde{F}(\omega)$ converges to $F(\omega)$ scaled by δ^{-1} (Wang and Pavlis, 2016).

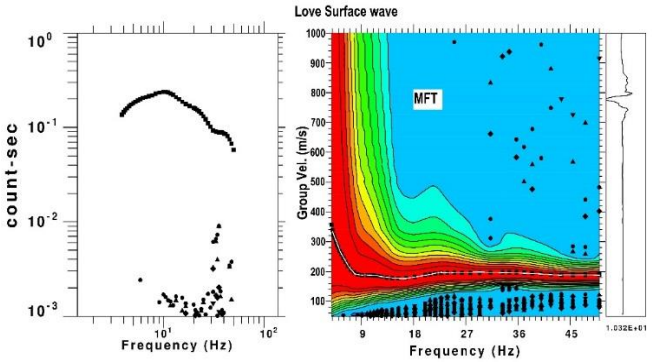

Figure 8: Multiple filter technique – MFT applied to the synthetic seismogram at a geophone (#22 in Figure 5) is shown.

The fundamental mode – FM group velocity curve obtained in Figure 8 is inverted for 1-D shear-wave velocity structure of the wave propagating media between the source and the receiver (i.e., geophone #22). The inversion result (red line) is illustrated in Figure 9 where the initial model received from Figure 7 is depicted by the blue dashed line. Since the theoretical model structure (Table 1) is 1-D, the inverted (red line – obtained from group velocity) and the initial (blue dashed line – obtained from phase velocity) model structures closely match as expected. However, the two shear-wave velocity structures are still slightly different from each other particularly below the 25-m depth. This is mainly because the group and phase velocities compared to each other have different resolution power changing with depth (Young et al., 2011). The theoretical (or observed) group velocity curve indicated by the triangular symbols in Figure 9 shows some fluctuation at short periods < 0.1 s (or high frequencies > 10 Hz). This is due to the first higher mode interfering with the fundamental mode in the mentioned period range (see the three arrows in Figure 6). This interference effect becomes less effective at faraway geophones from the source since the higher modes with short wavelengths are steadily attenuated with propagation distance.

We repeat the data processing illustrated in Figure 9 for the other geophone recordings in the array from geophone #15 to geophone #40, which yields 26 FM group velocity curves analogous to classical single-station approach. We apply the procedure defined in Eq. (2) to convert these single-station dispersion curves into a set of local dispersion curves at each grid point with constant spacing set to 2-m, which is the same with the geophone spacing. In the current design, the linear system in Eq. (2) has 26 rows consistent with the number of single-station (observed) group velocity curves and 26 columns corresponding to the number of grid points. Figure 10 illustrates the data processing scheme utilized in Eq. (2). Herein, Figure 10 is only representative, and the actual number of geophones and grid points changes according to the specific problem under consideration. The system in Eq. (2) is valid for one surface wave period and is repeatedly solved for every other surface wave period to construct the respective period dependent dispersion curve at each grid point.

$$\begin{bmatrix} 1&0&0&0&0&0&0&0&0&0&0&0 \\ 1&1&0&0&0&0&0&0&0&0&0&0 \\ 1&1&1&0&0&0&0&0&0&0&0&0 \\ \vdots & & & & & & & & & & & \\ 1&1&1&1&1&1&1&1&1&1&1&0 \\ 1&1&1&1&1&1&1&1&1&1&1&1 \end{bmatrix} \begin{bmatrix} S_1 \\ S_2 \\ S_3 \\ \vdots \\ S_{m-1} \\ S_m \end{bmatrix} \Delta x = \begin{bmatrix} \bar{S}_1 - S_0 \\ \bar{S}_2 - S_0 \\ \bar{S}_3 - S_0 \\ \vdots \\ \bar{S}_{m-1} - S_0 \\ \bar{S}_m - S_0 \end{bmatrix} x_0 + \begin{bmatrix} \bar{S}_1 \\ 2\bar{S}_2 \\ 3\bar{S}_3 \\ \vdots \\ (m-1)\bar{S}_{m-1} \\ m\bar{S}_m \end{bmatrix} \Delta x \quad (2)$$

where m is the number of geophones and grid points, $\bar{S}_i$ represents the single-station (observed) group slowness, and S_i stands for the group

slowness at a grid point attained by solving the linear system in Eq (2).

Eq. (2) can be solved by damped least squares method, i.e., $(\boldsymbol{A}^T\boldsymbol{A} + \lambda\boldsymbol{I})\boldsymbol{s} = \boldsymbol{A}^T\tilde{\boldsymbol{s}}$ where λ is the damping parameter used to subdue the noise effect, $\boldsymbol{A}$ with dimension (mxm) and lower triangular form is the system matrix, $\boldsymbol{s}$ is the unknown slowness vector, and $\tilde{\boldsymbol{s}}$ is the known slowness vector corresponding to the righthand side in Eq. (2). S_0 represents the average (group) slowness corresponding to the wave propagation media from the source to the first geophone (i.e., currently geophone #15) utilized in Eq. (2). We compute S_0 from the 1-D velocity-depth profile obtained from the inversion of the phase velocity curve shown in Figure 7. Alternatively, S_0 can be computed from the 1-D velocity structure obtained from the inversion of the group velocity curve at geophone #15. However, S_0 values attained from the latter approach may suffer from the higher mode interference especially at high frequencies (e.g., see Figure 9). Note that the lateral resolution in Figure 10 can be increased by decreasing the geophone spacing (i.e., Δx).

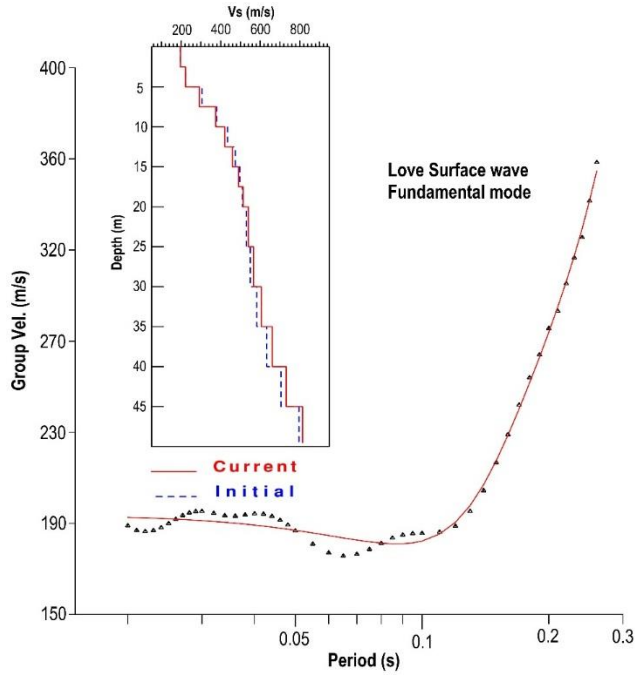

Figure 9: 1-D inversion result for the group velocity curve in Figure 8 is shown. Vs stands for the shear-wave velocity (m/s). The horizontal axis shows the period (s)

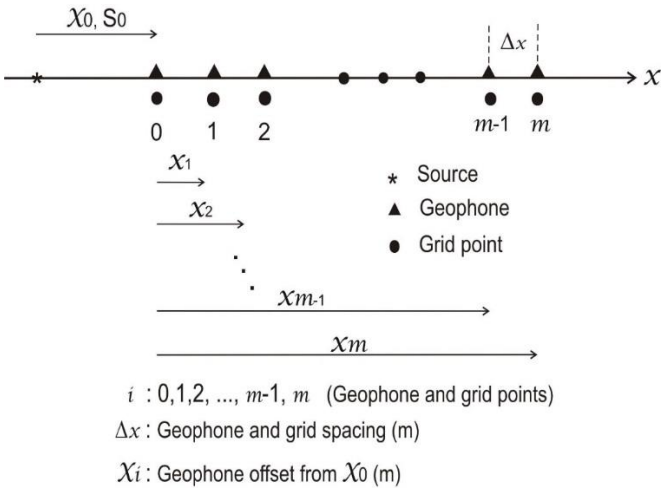

Figure 10: The data processing system designed to convert single-station group velocities at geophone locations into local group velocities at grid points is illustrated.

Figure 11 shows the cross-sectional result of Eq. (2) applied to the geophone recordings (see the check marks in Figure 5) each treated as a single station recording. The shear-wave velocities (m/s) of the multi-layered 1-D model structure (Table 1) are superimposed on the cross section along with the layer interfaces. A rich color scale is employed to show the change of the inverted shear-wave velocities with depth. The near surface layers are well resolved in terms of both layer thickness and shear-wave velocity since the high frequency (or short wavelength) FM surface wave energy can probe this depth range. The resolution is somewhat lower for the deeper layers since these layers are probed by gradually lower frequencies (or long wavelengths). The resolution loss is particularly evident for the interface sharpness between the layers. In the model structure, the shear-wave velocities steadily increase with depth and there exist some velocity jumps (mainly 50 m/s) across the layer interfaces. The velocity jump corresponding to the first interface (i.e., 150 m/s) at 5-m depth is well resolved while the other velocity jump with the same rate at 30-m depth is not resolved as sharp as in the model structure. In addition, the half-space velocity is estimated ~50 m/s lower than the actual velocity (850 m/s). For the other layers especially deeper ones the shear-wave velocities are estimated 10-20 m/s lower than the actual velocities.

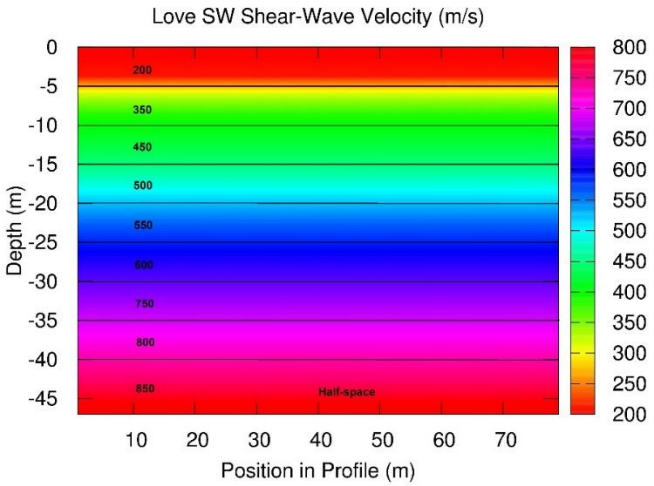

Figure 11: The cross section obtained for the shear-wave velocities in the model structure is shown. See the text for more explanation.

3.1.2 Resistivity modeling

We compute the theoretical apparent resistivity pseudo-section (i.e., forward modeling) of the multi-layered resistivity model in Table 1 for which we utilize the finite differences in the source code package distributed (Loke, 2014). The finite difference method is used with grid cells equal to one half the electrode spacing. The multiple electrode Pole-Pole array is used with 3-m electrode spacing. The number of electrodes is set to 44, and then the profile length is 129 m. In the numerical computations (i.e., apparent resistivity values), we consider the noise free conditions. In field applications, there exist three procedures used to explore the subsurface features, i.e., electrical horizontal profiling, electrical vertical profiling, and electrical vertical sounding (Coşkun, 1994).

The horizontal profiling is mainly conducted to explore the near surface properties of the underground where a fixed electrode spacing is used while the electrodes are moved from place to place to make a series of apparent resistivity measurements. However, with the latter profiling technique only limited stratigraphic information in the vertical direction is provided to the reader. In the vertical profiling, a range of inner electrode and electrode spacings are chosen. A profile is continually measured by increasing the electrode spacing. In this way, at each step deeper portions of the underground are measured to generate the respective apparent resistivity pseudo-section. The vertical electrical sounding (VES), which may be suitable for investigating the uniform horizontal layers, is used to explore the stratified media using electrode arrangements that include systematic increments of depth probing.

We estimate the true resistivity structure by inverting the apparent resistivity pseudo-section (Figure 12) where the source code package delivered is utilized (Loke, 2002; 2004). This algorithm employs least-squares inversion along with two-dimensional smoothing. A quasi-Newtonian technique is used to reduce the number of numerical calculations in the modeling (Loke and Barker, 1996). The current inversion technique is effective to estimate the layer thicknesses and resistivities particularly near the surface (Figure 13). The resistivities of

the multi-layered 1-D model structure (Table 1) are superimposed on the cross section along with the layer interfaces. A rainbow color scale is used to show the change of the inverted resistivities with depth.

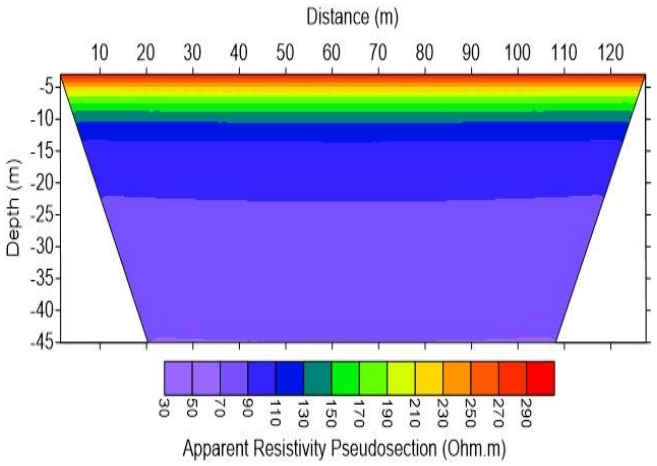

Figure 12: The resistivity cross section corresponding to the model structure in Table 1 is shown in terms of the apparent (observed) resistivity values.

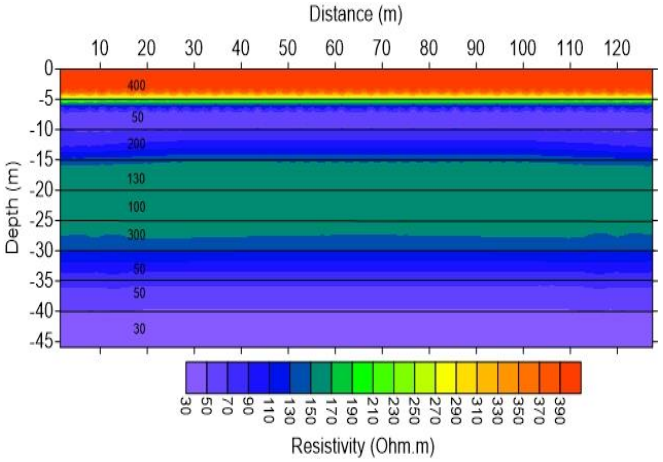

Figure 13: The resistivity cross section corresponding to the model structure in Table 1 is shown in terms of the true (inverted) resistivity values. See the text for more explanation.

In Figure 13, the inverted resistivity values deviate from the actual ones particularly at those depths from 10-m to 30-m where the resistivity quickly changes with depth. On the other hand, the thickness and resistivity of the first layer and the resistivity of the ninth layer (i.e., half-space) are well inverted (compare to Table 1). The yellow strip seen at 4-m is a false anomaly resulting from the inversion process. The layer thickness and the resistivity in the eighth layer is well resolved in the inversion, but the resistivity of the seventh layer, which has the same resistivity value with the eighth layer, is overestimated at ~120 Ω m instead of actual 50 Ω m. Among the other electrode arrangements reported in the literature (e.g., Wenner, Schlumberger, Dipole-Dipole) we have found the Pole-Pole arrangement most suitable for the modeling of the considered multilayered resistivity structure within the near surface Earth (Milsom, 2003).

4. Discussions

The current study focuses on numerical experiments performed on one-dimensional model structure. The Love surface wave data consists of only fundamental mode – FM and these higher modes are practically absent on the waveforms because of the source placed on the free surface. If the source depth is increased to a few meters (e.g., 5-m), then the higher modes (fundamental mode plus three higher modes) become visible on the phase velocity dispersion image as shown in Figure 14. Note that the second and third higher modes are only visible when the maximum frequency is revised to 100 Hz instead of 50 Hz considered above. The additional three higher modes besides the FM provide better vertical and horizontal resolution of the wave propagating media since then the short wavelengths probing the deeper Earth structure are considered in the velocity inversion. For instance, the FM at 8 Hz and the first higher mode at 20 Hz probe almost the same depth range, but the resolution power brought by the first higher mode is 2.5 (i.e., 20/8) times more than the FM (see the purple lines in Figure 14).

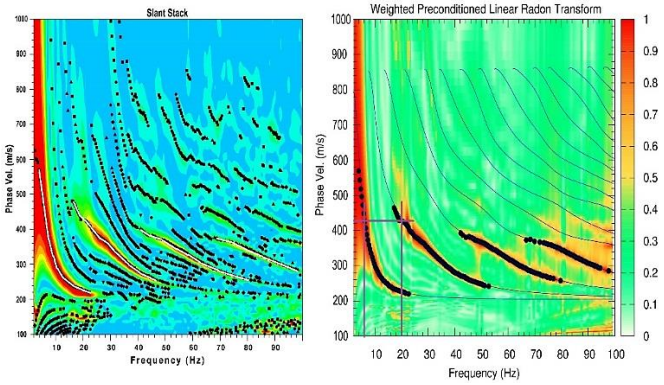

Figure 14: Multi-mode phase velocities in the model structure computed by setting the source depth to 5-m. The left panel corresponds to the method of slant stacking (white lines). In the right panel, the method of linear radon transform weighted and preconditioned is used (solid circles).

The real earth has multi-dimensional heterogeneities, which are high frequency embedded structures (i.e., inclusions such as cavity, sink hole, salt, fluid, melt, ore body). The embedding low frequency structure can be approximated by multiple layers with sub-horizontal interfaces. Herein we are primarily interested in the low frequency structures, but the current approach should also be effective on the high frequency embedded structures, especially when the higher modes are included in the modeling efforts. However, the Love surface wave higher modes come with some expense since one needs to set up the SH-wave source (see Figure 1) below the free surface level. To locally excavate the Earth as deep as 5-m (i.e., digging a trench) could be a solution. The latter procedure is expensive but rewarding.

In the numerical experiments, we did not consider the effect of the geophone impulse response. In case that the geophone impulse response shows the range of frequencies with amplitude and phase effects, then one needs to remove the instrument effect from the recordings so that only the ground motion is modelled for the velocity structure of the underground (Hons and Stewart, 2006). The field surface wave experiment typically utilizes 4.5 Hz geophone in which the instrument correction may be redundant for frequencies greater than 4.5 Hz (natural frequency) because of the flat response. If the latter is not valid, then the response curves provided by the manufacturer (i.e., amplitude and phase) can be considered to remove the instrument effect.

The current approach is based on isolating the different modes on the dispersion image. The higher modes may interfere with the fundamental mode – FM and the higher modes may interfere with each other (Dal Moro, 2020). In these cases, the mode isolation process could be quite difficult (e.g., see the right panel in Figure 4). The multi-mode phase velocity dispersion curves obtained by slant stacking or linear radon transform (e.g., see Figure 14), which are comparatively free of mode interference effects (e.g., see the left panel in Figure 4), could be used to estimate the locations of the multi-mode group velocity curves on the dispersion image. An alternative method could be full waveform inversion, but this approach requires source information, excessive computational time (CPU), and may be incompetent when the wave propagating media includes strong heterogeneities (Levshin and Panza, 2006).

A contemporary resistivity application in the field employs multi-electrode measurement system along with a commonly used traditional electrode array (e.g., Pole-Pole, Dipole-Dipole, Wenner, Schlumberger), which is the approach adopted herein. More recent field applications (Coşkun et al., 2016a, 2016b) have started using multi-channel resistivity acquisition systems, which are more competent since for each current injection into the ground all other electrodes are used to measure the voltages corresponding to all electrode arrays. Therefore, more useful data are efficiently collected drastically increasing the inversion quality. Herein, in the resistivity modeling, we employ 44 electrodes, 3-m electrode spacing and 129-m profile length. Both vertical and lateral resolution in the inverted resistivity can be increased by adjusting all these three parameters to new values, i.e., the number of electrodes increased to (for instance) 101, electrode spacing decreased to 2-m, and the profile length increased to hundreds of meters. Currently, we do not have computational power to perform the resistivity modeling beyond what is presented.

Different geophysical methods (e.g., seismic, resistivity, gravity) are sensitive to different physical properties of the underground (i.e., velocity, conductivity, density). A combination of different geophysical methods may be useful to distinguish the lithologies. A combination of seismic and resistivity methods may help resolve circulation of the fluids within the Earth. A low seismic velocity and high electrical conductivity may correspond to the presence of fluids (Iwamori et al., 2021). A low seismic velocity and high electrical resistivity may indicate the existence of voids while a high seismic velocity and low electrical resistivity may result from the occurrence of ore deposits. Therefore, multiple geophysical methods, which are jointly utilized, may be more advantageous than that these methods are applied alone.

Conflict of Interest

The authors state that there is no conflict of interest.

Acknowledgements

We are grateful to the anonymous reviewers for critically reviewing the manuscript.

References

Amaya, A.G., Dahlin, T., Barmen, G., Rosberg, J.E., 2016. Electrical Resistivity Tomography and Induced Polarization for Mapping the Subsurface of Alluvial Fans: A Case Study in Punata (Bolivia). Geosciences, 6, Pp. 51.

Bačić, M., Librić, L., Kaćunić, D.J., Kovačević, M.S., 2020. The Usefulness of Seismic Surveys for Geotechnical Engineering in Karst: Some Practical Examples. Geosciences, 10, Pp. 406.

Bitri, A., Samyn, K., Brûlé, S., Javelaud, E.H., 2013. Assessment of ground compaction using multi-channel analysis of surface wave data and cone penetration tests. Near Surface Geophysics, 11, Pp. 683-690.

Borcherdt, R.D., 2012. Vs30–A site-characterization parameter for use in building Codes, simplified earthquake resistant design, GMPEs, and ShakeMaps. The 15th World Conference on Earthquake Engineering.

Çakır, Ö., 2018. Seismic crust structure beneath the Aegean region in southwest Turkey from radial anisotropic inversion of Rayleigh and Love surface waves. Acta Geophysica, 66, Pp. 1303–1340.

Çakır, Ö., 2019. Love and Rayleigh Waves Inverted for Vertical Transverse Isotropic Crust Structure beneath the Biga Peninsula and the surrounding area in NW Turkey. Geophysical Journal International, 216, Pp. 2081-2105.

Çakır, Ö., Coşkun, N., Erduran, M., 2019. Nevşehir castle region in Turkey interpreted by the use of seismic surface wave and electrical resistance measurements together. Pakistan Journal of Geology, 3, Pp. 9-19.

Carbajal, M.R., 2014. Time-lapse and probabilistic inversion strategies for plane-wave electromagnetic methods, PhD Dissertation, Sciences of the Universe, Université de Lausanne.

Cardarelli, E., Donno, G.D., 2017. Multidimensional electrical resistivity survey for bedrock detection at the Rieti Plain (Central Italy). Journal of Applied Geophysics, 141, Pp. 77-87.

Chianga, C.W., Yang, Z.X., Chen, C.C., Yeh, E.C., Chen, C.S., Wang, C.Y., 2021. Potential geothermal structure inferred from the electrical resistivity and seismic reflection models in the western Ilan Plain, NE Taiwan. Geothermics, 94, Pp. 102124.

Colella, A., Lapenna, V., Rizzo, E., 2004. High-resolution imaging of the High Agri Valley Basin (Southern Italy) with electrical resistivity tomography. Tectonophysics, 386, Pp. 29–40.

Coşkun, N., 1994. A comparison of configuration arrays for the resistivity and induced polarisation methods and a direct interpretation technique for vertical profiling field data, Ph.D. Dissertation, University of York.

Coşkun, N., Çakır, Ö., Erduran, M., Kutlu, Y.A., Çetiner, Z.S., 2016a. Preliminary investigation of underground settlements of Nevşehir Castle region using 2.5-D electrical resistivity tomography: Cappadocia, Turkey. Arabian Journal of Geosciences, 9, Pp. 717.

Coşkun, N., Çakır, Ö., Erduran, M., Kutlu, Y.A., Çetiner, Z.S., 2016b. A potential landslide area investigated by 2.5D electrical resistivity tomography: case study from Çanakkale, Turkey. Arabian Journal of Geosciences, 9, Pp. 6.

Crook, N., Binley, A., Knight, R., Robinson, D.A., Zarnetske, J., Haggerty, R., 2008. Electrical resistivity imaging of the architecture of substream sediments. Water Resources Research, 44, Pp. W00D13.

Dal Moro, G., 2020. The magnifying effect of a thin shallow stiff layer on Love waves as revealed by multi-component analysis of surface waves. Scientific Reports, 10, Pp. 9071.

Dumont, G., Robert, T., Marck, N., Nguyen, F., 2017. Assessment of multiple geophysical techniques for the characterization of municipal waste deposit sites. Journal of Applied Geophysics, 145, Pp. 74-83.

Dziewonski, A., Bloch, S., Landisman, M. 1969. A technique for analysis of transient seismic signals. Bulletin of Seismological Society of America, 59, Pp. 427-444.

Erduran, M., Çakır, Ö., Tezel, T., Şahin, Ş., Alptekin, Ö., 2007. Anatolian surface waves evaluated at GEOFON station ISP Isparta, Turkey. Tectonophysics, 434, Pp. 39-54.

Furumura, M., Sasatani, T., Furumura, T., 1997. Generation of Basin-Induced Surface Waves Observed in the Tokachi Basin, Hokkaido, Japan. Journal of Physics and Earth, 45, Pp. 287-305.

Gao, L., Xia, J., Pan, Y., Xu, Y., 2016. Reason and Condition for Mode Kissing in MASW Method. Pure and Applied Geophysics, 173, Pp. 1627–1638.

Gao, L., Pan, Y., Tian, G., Xia, J., 2018. Estimating Q Factor from Multi-mode Shallow-Seismic Surface Waves. Pure and Applied Geophysics, 175, Pp. 2609–2622.

Gaždová, R., Kolínský, P., Vilhelm, J., Valenta, J., 2015. Combining surface waves and common methods for shallow geophysical survey. Near Surface Geophysics, 13, Pp. 19–32.

Gresse, M., Vandemeulebrouck, J., Byrdina, S., Chiodini, G., Revil, A., Johnson, T.C., Ricci, T., Vilardo, G., Mangiacapra, A., Lebourg, T., Grangeon, J., Bascou, P., Metral, L., 2017. Three-Dimensional Electrical Resistivity Tomography of the Solfatara Crater (Italy): Implication for the Multiphase Flow Structure of the Shallow Hydrothermal System. Journal of Geophysical Journal: Solid Earth, 122, Pp. 8749-8768.

Haines, S.S., 2007. A hammer-impact, aluminum, shear-wave seismic source, U.S. Geological Survey Open-File Report 2007-1406, Pp. 5.

Herrmann, R.B., 1973. Some aspects of band-pass filtering of surface waves. Bulletin of Seismological Society of America, 63, Pp. 663-671.

Herrmann, R.B., 2002. Computer programs in seismology, version 3.30. St. Louis University, Missouri.

Hollender, F., Cornou, C., Dechamp, A., Oghalaei, K., Renalier, F., Maufroy, E., Burnouf, C., Thomassin, S., Wathelet, M., Bard, P.-Y., Boutin, V., Desbordes, C., Douste-Bacqué, I., Foundotos, L., Guyonnet-Benaize, C., Perron, P., Régnier, J., Roullé, A., Langlais, M., Sicilia, D., 2018. Characterization of site conditions (soil class, VS30, velocity profiles) for 33 stations from the French permanent accelerometric network (RAP) using surface wave methods. Bulletin of Earthquake Engineering, 16, Pp. 2337–2365.

Hons, M.S., Stewart, R.R., 2006. Transfer functions of geophones and accelerometers and their effects on frequency content and wavelets, CREWES Research Report – Pp. 18.

Issah, M.M., Aning, A.A., Noye, R.M., Mainoo, P.A., 2018. Prospecting for Groundwater Using the Continuous Vertical Electrical Sounding Method. European Scientific Journal, 14, Pp. 67.

Iwamori, H., Ueki, K., Hoshide, T., Sakuma, H., Ichiki, M., Watanabe, T., Nakamura, M., Nakamura, H., Nishizawa, T., Nakao, A., Ogawa, Y., Kuwatani, T., Nagata, K., Okada, T., Takahashi, E., 2021. Simultaneous of Seismic Velocity and Electrical Conductivity in the Crust and the Analysis Uppermost Mantle: A Forward Model and Inversion Test Based on Grid Search. Journal of Geophysical Research: Solid Earth, 126, Pp. e2021JB022307.

Jin, G., Gaherty, J.B., 2015. Surface wave phase-velocity tomography based on multichannel cross-correlation. Geophysical Journal International, 201, Pp. 1383–1398.

Kana, J.D., Djongyang, N., Raïdandi, D., Nouck, P.N., Dadjé, A., 2015. A review of geophysical methods for geothermal exploration. Renewable and Sustainable Energy Reviews, 44, Pp. 87-95.

Kanlı, A.I., Tildy, P., Prónay, Z., Pınar, A., Hermann, L., 2006. VS30 mapping and soil classification for seismic site effect evaluation in Dinar region, SW Turkey. Geophysical Journal International, 165, Pp. 223–235.

Kasamatsu, K., Yamanaka, H., Sakai, S., 2021. Inversion of Love waves in earthquake ground motion records for two-dimensional S-wave velocity model of deep sedimentary layers. Earth, Planets and Space, 73, Pp. 17.

Kowalczyk, S., Zawrzykraj, P., Maślakowski, M., 2017. Application of the electrical resistivity method in assessing soil for the foundation of bridge structures: a case study from the Warsaw environs, Poland. Acta Geodynamica et Geomaterialia, 14, Pp. 221–234.

Lawton, D.C., Gallant, E.V., Bertram, M.B., Hall, K.W., Bertram, K.L., 2013. A new S-wave seismic source, CREWES Research Report – Pp. 25.

Levshin, A.L., Panza, G.F., 2006. Caveats in Multi-modal Inversion of Seismic Surface Wavefields. Pure and Applied Geophysics, 163, Pp. 1215–1233.

Loke M.H., Barker R.D., 1996. Rapid least-squares inversion of apparent resistivity pseudosections using a quasi-Newton method. Geophysical Prospecting, 44, Pp. 131-152.

Loke, M.H., 1997. Electrical imaging surveys for environmental and engineering studies, a practical guide to 2-D and 3-D surveys: RES2DINVand RES2MOD manual.

Loke, M.H., 2002. RES2DINV ver. 3.50. Rapid 2-D Resistivity and IP Inversion Using the Least Square Method.

Loke, M.H., 2004. Tutorial: 2-D and 3-D electrical imaging surveys, Geotomo Software, Penang, Malaysia. www.geotomosoft.com

Loke, M.H., 2014. RES2DMOD ver. 3.01: Rapid 2D resistivity forward modeling using the finite-difference and finite-element methods, Geotomo Software, Malaysia, Pp. 23.

Luo, Y., Xia, J., Miller, R.D., Xu, Y., Liu, J., Liu, Q., 2008. Rayleigh-Wave Dispersive Energy Imaging Using a High-Resolution Linear Radon Transform. Pure and Applied Geophysics, 165, Pp. 903–922.

Mahvelati, S., Coe, J.T., Nyquist, J.E., 2021. Characterizing the Effects of Survey Parameters on Experimental Love Wave Multichannel Analysis of Surface Wave (MASW) Data. Pure and Applied Geophysics, 178, Pp. 2933–2952.

McMechan, G.A., Yedlin, M.J., 1981. Analysis of dispersive waves by wave field transformation. Geophysics, 46, Pp. 869–874.

Mi, B., Jianghai Xia, J., Bradford, J.H., Shen, C., 2020. Estimating Near-Surface Shear-Wave-Velocity Structures Via Multichannel Analysis of Rayleigh and Love Waves: An Experiment at the Boise Hydro geophysical Research Site. Surveys in Geophysics, 41, Pp. 323–341.

Milsom, J., 2003. Field Geophysics, The Geological Field Guide Series, Third Edition, Willey, England.

Mokhtar, T.A., Herrmann, R.B., Russell, D.R., 1988. Seismic velocity and Q model for the shallow structure of the Arabian shield from short-period Rayleigh waves. Geophysics, 53, Pp. 1379-1387.

Nishida, K., Kawakatsu, H., Obara, K., 2008. Three-dimensional crustal S wave velocity structure in Japan using microseismic data recorded by Hi-net tiltmeters. Journal of Geophysical Research, 113, Pp. B10302.

Ojo, A.O., Ni, S., Li, Z., 2017. Crustal radial anisotropy beneath Cameroon from ambient noise tomography. Tectonophysics, 696–697, Pp. 37–51.

Onyebueke, E.O., Manzi, M.S.D., Durrheim, R.J., 2018. High-resolution shallow reflection seismic integrated with other geophysical methods for hydrogeological prospecting in the Nylsvley Nature Reserve, South Africa. Journal of Geophysics and Engineering, 15, Pp. 2658–2673.

Orlando, L., 2013. Some considerations on electrical resistivity imaging for characterization of waterbed sediments. Journal of Applied Geophysics, 95, Pp. 77–89.

Palacky, G., 1988. Resistivity characteristics of geologic targets. Electromagnetic Methods in Applied Geophysics, 1, Pp. 53–129.

Pan, Y., Gao, L., Bohlen, T., 2019. High-Resolution Characterization of Near-Surface Structures by Surface-Wave Inversions: From Dispersion Curve to Full Waveform. Surveys in Geophysics, 40, Pp. 167–195.

Pan, Y., Gao, L., Shigapov, R., 2020. Multi-objective waveform inversion of shallow seismic wavefields. Geophysical Journal International, 220, Pp. 1619–1631.

Pancha, A., Apperley, R.A., 2021. Multidisciplinary site investigations: refraction microtremor surveys. Journal of Seismology. https://doi.org/10.1007/s10950-021-10019-y

Park, C.B., Ivanove, J., Miller, R.D., Xia, J., Ryden, N., 2001. Seismic investigation of pavements by MASW method – geophone approach, Proc. SAGEEP 2001, Denver, CO.

Pawlik, Ł., Kasprzak, M., 2018. Regolith properties under trees and the biomechanical effects caused by tree root systems as recognized by electrical resistivity tomography (ERT). Geomorphology, 300, Pp. 1-12.

Poblet, J., Lisle, R.J., 2011. Kinematic Evolution and Structural Styles of Fold-and-Thrust Belts. Geological Society, London, Special Publications, 349, Pp. 1–24.

Roche, V., Childs, C., Madritsch, H., Camanni, G., 2020. Layering and structural inheritance controls on fault zone structure in three dimensions: a case study from the northern Molasse Basin, Switzerland. Journal of the Geological Society, 177, Pp. 493–508.

Ronczka, M., Hellman, K., Günther, T., Wisén, R., Dahlin, T., 2017. Electric resistivity and seismic refraction tomography: a challenging joint underwater survey at Äspö Hard Rock Laboratory. Solid Earth, 8, Pp. 671–682.

Schwardt, M., Köhn, D., Wunderlich, T., Wilken, D., Seeliger, M., Schmidts, T., Brückner, H., Başaran, S., Rabbel, W., 2020. Characterization of silty to fine-sandy sediments with SH waves: full waveform inversion in comparison with other geophysical methods. Near Surface Geophysics, 18, Pp. 217-248.

Senkaya, G.V., Senkaya, M., Karsli, H., Güney, R., 2020. Integrated shallow seismic imaging of a settlement located in a historical landslide area. Bulletin of Engineering Geology and the Environment, 79, Pp. 1781–1796.

Shapiro, N.M., Singh, S.K., Almora, D., Ayala, M., 2001. Evidence of the dominance of higher-mode surface waves in the lake-bed zone of the Valley of Mexico. Geophysical Journal International, 147, Pp. 517–527.

Silahtar, A., Kanbur, M.Z., Beyhan, G., 2020. Investigation of a sedimentary basin by using gravity and seismic reflection data in the Isparta basin, southwestern Turkey. Bulletin of Engineering Geology and the Environment, 79, Pp. 3971–3988.

Silahtar, A., Kanbur, M.Z., 2021. 1D nonlinear site response analysis of the Isparta Basin (Southwestern Turkey) with surface wave (ReMi) and borehole data. Environmental Earth Sciences, 80, Pp. 268.

Stummer, P., Maurer, H., Horstmeyer, H., Green, A.G., 2002. Optimization of DC resistivity data acquisition: real-time experimental design and a new multielectrode system. IEEE Transactions on Geoscience and Remote Sensing, 40, Pp. 2727–2735.

Thitimakorn, T., Raenak, T., 2016. NEHRP Site Classification and Preliminary Soil Amplification Maps of Lamphun City, Northern Thailand. Open Geosciences, 8, Pp. 538–547.

Troiano, A., Isaia, R., Di Giuseppe, M.G., Tramparulo, F.D.A., Vitale, S., 2019. Deep Electrical Resistivity Tomography for a 3D picture of the most active sector of Campi Flegrei caldera. Scientific Reports, 9, Pp. 15124.

Vanneste, M., Madshus, C., Socco, V.L., Maraschini, M., Sparrevik, P.M., Westerdahl, H., Duffaut, K., Skomedal, E., Bjørnarå, T.I., 2011. On the use of the Norwegian Geotechnical Institute's prototype seabed-coupled shear wave vibrator for shallow soil characterization – I. Acquisition and processing of multimodal surface waves. Geophysical Journal International, 185, Pp. 221–236.

Wang, Y., Pavlis, G.L., 2016. Generalized iterative deconvolution for

receiver function estimation. Geophysical Journal International, 204, Pp. 1086–1099.

Wright, C.L., 2012. SH-wave refraction and reflection investigation of quaternary geology-Central United States seismic observatory, Theses and Dissertations-Earth and Environmental Sciences, 6.

Xia, J., Miller, R.D., Park, C.B., 1999. Estimation of near-surface shear-wave velocity by inversion of Rayleigh waves. Geophysics, 64 (3), Pp. 691–700.

Xia, J., Xu, Y., Luo, Y., Miller, R.D., Cakir, R., Zeng, C., 2012. Advantages of using Multichannel Analysis of Love Waves (MALW) to estimate near-surface shear-wave velocity. Surveys in Geophysics, 33, Pp. 841–860.

Xu, H., Beghein, C., 2019. Measuring higher mode surface wave dispersion using a transdimensional Bayesian approach. Geophysical Journal International, 218, Pp. 333–353.

Yan, Y., Wang, Z., Li, J., Huai, N., Liang, Y., Song, S., Zhang, J., Zhang, L., 2020. Elastic SH- and Love-wave Full-Waveform Inversion for shallow shear wave velocity with a preconditioned technique. Journal of Applied Geophysics, 173, Pp. 103947.

Yin, X., Xu, H., Mi, B., Hao, X., Wang, P., Zhang, K., 2020. Joint inversion of Rayleigh and Love wave dispersion curves for improving the accuracy of near-surface S-wave velocities. Journal of Applied Geophysics, 176, Pp. 103939.

Young, M.K., Rawlinson, N., Arroucau, P., Reading, A.M., Tkalčić, H., 2011. High-frequency ambient noise tomography of southeast Australia: New constraints on Tasmania's tectonic past. Geophysical Research Letters, 38, Pp. L13313.

Yuan, J., Zhu, J., Kim, C., 2014. Comparison of SASW and MASW methods using MSOR approach – a case study. International Journal of Geotechnical Engineering, 8, Pp. 233-238.